



Computer modeling of lithium phosphate and thiophosphate electrolyte materials

N.A.W. Holzwarth*, N.D. Lepley, Yaojun A. Du¹

Department of Physics, Wake Forest University, Winston-Salem, NC 27109, USA

ARTICLE INFO

Article history:

Received 8 July 2010

Accepted 16 August 2010

Available online 28 September 2010

Keywords:

Solid electrolyte
Computer modeling
Lithium phosphate
Lithium thiophosphate

ABSTRACT

In this work, several lithium phosphate and thiophosphate materials are modeled to determine their optimized lattice structures, their total energies, and their electronic structures. Included in this study are materials characterized by isolated phosphate and thiophosphate groups – Li_3PS_4 and Li_3PO_4 and materials characterized by phosphate and thiophosphate dimers – $\text{Li}_4\text{P}_2\text{S}_6$ and $\text{Li}_4\text{P}_2\text{O}_6$ and $\text{Li}_4\text{P}_2\text{S}_7$ and $\text{Li}_4\text{P}_2\text{O}_7$. In addition, the superionic conducting material $\text{Li}_7\text{P}_3\text{S}_{11}$ is also modeled as are recently discovered crystalline argyrodite materials Li_7PS_6 and $\text{Li}_6\text{PS}_5\text{Cl}$. A comparison of Li ion vacancy migration in $\text{Li}_4\text{P}_2\text{S}_7$ and $\text{Li}_4\text{P}_2\text{O}_7$ shows the migration energy barriers in the thiophosphate to be smaller (less than one-half) than in the phosphate.

© 2010 Elsevier B.V. All rights reserved.

1. Introduction

Lithium phosphorous oxynitride (LiPON) films were developed at Oak Ridge National Laboratory [1–4] as very promising solid-state electrolytes for use in rechargeable batteries and other applications. The films have compositions close to that of crystalline Li_3PO_4 and ionic conductivities of $10^{-6} \text{ S cm}^{-1}$. In previous work [5–9], we investigated detailed mechanisms for Li ion migration in idealized models of LiPON based on Li_3PO_4 and related phosphonitrides. In those materials we found that Li ions can diffuse by vacancy and interstitial mechanisms with migration energies of 0.3–0.7 eV. In the present work, we report preliminary results for extending this modeling study to lithium thiophosphate materials which have recently received attention as promising candidates for solid-state electrolytes [10–19] where increased ionic conductivity as large as $10^{-3} \text{ S cm}^{-1}$ has been reported.

In Section 2, the computational methods are briefly described. In Section 3, results are presented for the optimized structures of the materials, comparing corresponding phosphates and thiophosphates when possible. In Section 4, heats of formation are presented and compared with available experimental measurements. In Section 5, partial densities of states are presented in order to develop qualitative pictures of the bonding properties of the materials. In Section 6, ion migration energies are

presented for one of the phosphate and thiophosphate materials. A summary and some conclusions are presented in Section 7.

2. Computational methods

The computational methods used in this work were the same as those used in our previous studies of electrolytes related to LiPON. In Ref. [9], the choice of calculational parameters and the validation of the calculational methods are presented. Briefly, we used density functional theory [20,21] to treat the electronic states and the Born-Oppenheimer approximation to treat the atomic positions $\{\mathbf{R}^a\}$, resulting in a determination of the “total energy” $E(\{\mathbf{R}^a\})$ of the system. The local density approximation (LDA) [22] was used for the exchange-correlation functional. Most of the computations were carried out using the *PWscf* package [23]; while a few calculations were performed using the *abinit* [24] and *pwppaw* [25] packages as well. Visualizations were constructed using the *OpenDX* [26] and *XCrySDEN* [27] software packages.

Starting from experimental information for each material or a related material, restricted optimization of the total energy $E(\{\mathbf{R}^a\})$ with respect to the atomic positions $\{\mathbf{R}^a\}$ and unit cell parameters allows us to determine stable and meta-stable structures presented in Section 3 and to estimate the heat of formation (ΔH) presented in Section 4. For each meta-stable structure, a qualitative picture of the valence state distribution can be determined from the averaged partial densities of states $\langle N^a(E) \rangle$ presented in Section 5. In addition, migration energies (E_m) for Li ion migration were estimated using the “nudged elastic band” (NEB) method [28–30], presented in Section 6.

* Corresponding author. Tel.: +1 336 758 5510; fax: +1 336 758 6142.

E-mail address: natalie@wfu.edu (N.A.W. Holzwarth).

¹ ICAMS, Ruhr-Universität, 44780 Bochum, Germany.

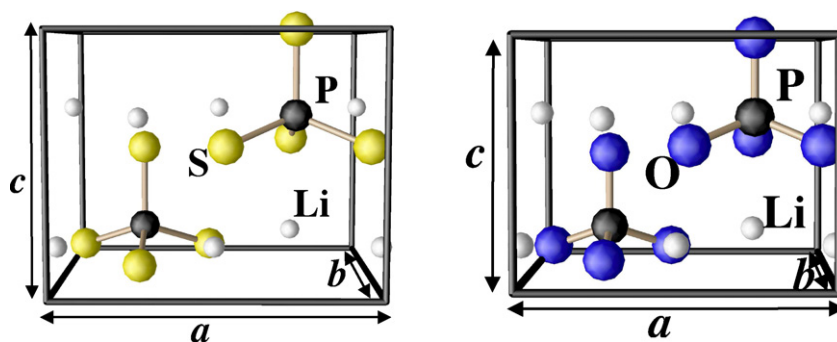


Fig. 1. Ball and stick diagrams for unit cells of Li_3PS_4 (left) and Li_3PO_4 (right) in the $Pmn2_1$ structure.

3. Simulated crystalline structures [31]

3.1. Li_3PS_4 and Li_3PO_4

Li_3PS_4 and Li_3PO_4 are characterized by isolated phosphate or thiophosphate groups. Li_3PO_4 has been reported in two different orthorhombic crystalline forms – the β form [32] has symmetry $Pmn2_1$ (#31) and the γ form [33] has symmetry $Pnma$ (#62). In our previous work [6] we found that the β form is more stable by 0.03 eV per formula unit, while more experimental results are reported for the γ form. The crystal structure of Li_3PS_4 was reported by Mercier et al. [34] to have an orthorhombic symmetry $Pnma$ (#62) which differs from γ - Li_3PO_4 structure because of different site occupancies, some of which are fractional. We determined optimized total energies for Li_3PS_4 in several approximations to the Mercier structure and in the β and γ structures of Li_3PO_4 , and found the lowest energy structure to be that of β - Li_3PO_4 structure. Our results indicate this structure to be more stable than the most stable approximation to the Mercier structure by 0.1 eV per formula unit and more stable than the γ - Li_3PO_4 structure by 0.2 eV per formula unit. The comparison of Li_3PS_4 and Li_3PO_4 in the β - Li_3PO_4 is illustrated in Fig. 1 and the optimized lattice parameters determined by our simulations are compared with experiment in Table 1. As reported earlier [6] the calculated lattice constants are systematically smaller than experiment as expected for calculations of this type, while the relative size parameters of the lattice, particularly the fractional coordinates are well modeled by the calculations. The lattice parameters of Li_3PS_4 are found to be roughly 25% larger than those of Li_3PO_4 and the fractional coordinates are quite similar for the two structures.

3.2. Li_7PS_6 and $\text{Li}_6\text{PS}_5\text{Cl}$

There has been a number of recent studies of lithium thiophosphate materials with additional sulfur and lithium ions in a structure associated with the mineral argyrodite [35–37]. The high

Table 1

Lattice parameters for Li_3PO_4 and Li_3PS_4 in the β - Li_3PO_4 structure, comparing the experimental results (“exp”) of Ref. [32] with the optimized structures (“cal”) found in this work (using the same crystal conventions as in Ref. [6]).

	a (Å)	b (Å)	c (Å)
Li_3PO_4 (exp)	6.12	5.24	4.86
Li_3PO_4 (cal)	6.01	5.15	4.76
Li_3PS_4 (cal)	7.57	6.44	6.06

Atom	Fractional coordinates – (x, y, z)		
	Li_3PO_4 (exp)	Li_3PO_4 (cal)	Li_3PS_4 (cal)
Li (4b)	(0.248, 0.328, 0.986)	(0.247, 0.328, 0.993)	(0.243, 0.315, 1.000)
Li (2a)	(0.500, 0.843, 0.989)	(0.500, 0.838, 0.992)	(0.500, 0.849, 0.986)
P (2a)	(0.000, 0.824, 0.000)	(0.000, 0.827, 0.000)	(0.000, 0.817, -0.001)
O/S (4b)	(0.208, 0.687, 0.896)	(0.211, 0.685, 0.893)	(0.221, 0.668, 0.889)
O/S (2a)	(0.000, 0.105, 0.900)	(0.000, 0.112, 0.896)	(0.000, 0.115, 0.884)
O/S (2a)	(0.500, 0.181, 0.817)	(0.500, 0.178, 0.825)	(0.500, 0.190, 0.837)

Li ion conductivity observed [38] in these materials is associated with high-temperature crystalline forms having multiple fractional occupancy sites. However, these materials also have ordered low-temperature structures which we have modeled in this work. The low-temperature structure of Li_7PS_6 has been found [35] to be $Pna2_1$ (#33). The low-temperature structure of $\text{Li}_6\text{PS}_5\text{Cl}$ has not been reported, but it is reasonable to assume that it is similar to that reported [36] for $\text{Li}_6\text{PS}_5\text{I}$ which forms a monoclinic structure with Cc (#9) symmetry. The calculations optimized the Li_7PS_6 and $\text{Li}_6\text{PS}_5\text{Cl}$ structures and the results are illustrated in Fig. 2. For Li_7PS_6 there are two unbounded S ions associated with each thiophosphate group and for $\text{Li}_6\text{PS}_5\text{Cl}$ there is one unbounded S ion and one unbounded Cl ion for each thiophosphate group. The optimized lattice parameters for these materials are presented in Table 2. Again we find the calculated lattice constants to be systematically too small, while the fractional coordinates are in reasonably good agreement with experiment. In the case of Li_7PS_6 , the X-ray data could not directly determine the fractional coordinates, but

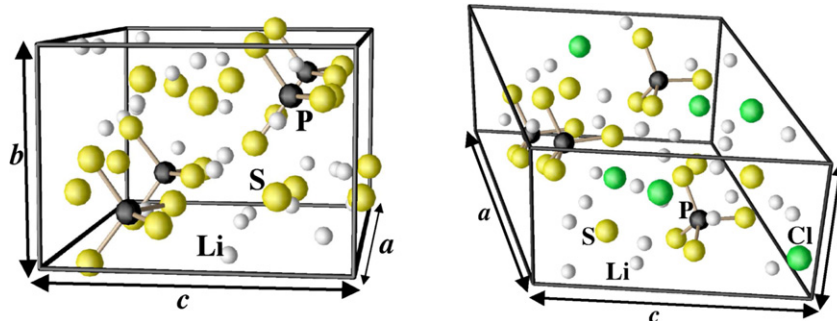


Fig. 2. Ball and stick diagrams for unit cells of Li_7S_6 in the $Pna2_1$ structure (left) and $\text{Li}_6\text{S}_5\text{I}$ in the Cc structure (right).

Table 2

(A) Lattice parameters for low-temperature form of Li_7PS_6 in the $Pna2_1$ structure comparing the experimental results of Ref. [35] with the calculational results. (B) Lattice parameters for low-temperature form of $\text{Li}_6\text{PS}_5\text{Cl}$ in the Cc structure comparing the experimental results of Ref. [36] for $\text{Li}_6\text{PS}_5\text{I}$ with the calculational results for the Cl material.

A				
	a (Å)	b (Å)	c (Å)	
Li_7PS_6 (exp)	14.08	6.92	9.96	
Li_7PS_6 (cal)	13.82	6.90	9.62	
Atom	Fractional coordinates – (x, y, z)			
	Li_7PS_6 (exp)		Li_7PS_6 (cal)	
Li (1)	(0.238, 0.464, 0.998)		(0.228, 0.533, 0.948)	
Li (2)	(0.771, 0.416, 0.047)		(0.777, 0.401, 0.048)	
Li (3)	(0.294, 0.768, 0.745)		(0.314, 0.784, 0.734)	
Li (4)	(0.967, 0.092, 0.088)		(0.971, 0.167, 0.097)	
Li (5)	(0.551, 0.936, 0.928)		(0.541, 0.949, 0.946)	
Li (6)	(0.857, 0.021, 0.365)		(0.912, 0.050, 0.409)	
Li (7)	(0.377, 0.830, 0.270)		(0.376, 0.848, 0.257)	
P	(0.124, 0.753, 0.250)		(0.118, 0.775, 0.245)	
S (1)	(0.002, 0.757, 0.118)		(0.000, 0.793, 0.116)	
S (2)	(0.251, 0.251, 0.624)		(0.262, 0.270, 0.624)	
S (3)	(0.379, 0.504, 0.876)		(0.391, 0.510, 0.873)	
S (4)	(0.881, 0.505, 0.873)		(0.886, 0.468, 0.866)	
S (5)	(0.125, 0.718, 0.735)		(0.142, 0.698, 0.761)	
S (6)	(0.385, 0.740, 0.506)		(0.372, 0.762, 0.499)	
B				
	a (Å)	b (Å)	c (Å)	β
$\text{Li}_6\text{PS}_5\text{I}$ (exp)	12.32	7.14	12.45	109.5°
$\text{Li}_6\text{PS}_5\text{Cl}$ (cal)	11.96	6.93	11.64	110.3°
Atom	Fractional coordinates – (x, y, z)			
	$\text{Li}_6\text{PS}_5\text{I}$ (exp)		$\text{Li}_6\text{PS}_5\text{Cl}$ (cal)	
Li (1)	(0.985, 0.305, 0.371)		(1.004, 0.363, 0.408)	
Li (2)	(0.765, 0.017, 0.885)		(0.841, 0.009, 0.878)	
Li (3)	(0.830, 0.515, 0.385)		(0.799, 0.533, 0.373)	
Li (4)	(0.709, 0.740, 0.066)		(0.684, 0.749, 0.025)	
Li (5)	(0.980, 0.953, 0.131)		(0.982, 0.913, 0.169)	
Li (6)	(0.997, 0.415, 0.679)		(0.976, 0.459, 0.664)	
P	(0.747, 0.743, 0.624)		(0.745, 0.764, 0.621)	
S (1)	(0.691, 0.983, 0.672)		(0.680, 0.995, 0.177)	
S (2)	(0.685, 0.480, 0.180)		(0.678, 0.484, 0.166)	
S (3)	(0.921, 0.248, 0.174)		(0.927, 0.228, 0.203)	
S (4)	(0.692, 0.734, 0.444)		(0.701, 0.782, 0.435)	
S (5)	(0.872, 0.248, 0.490)		(0.871, 0.270, 0.500)	
I/Cl	(-0.004, 0.747, 0.371)		(-0.018, 0.714, 0.354)	

Table 3

Lattice parameters of $\text{Li}_4\text{P}_2\text{S}_6$ (compared with the experimental measurements of Ref. [39]) and $\text{Li}_4\text{P}_2\text{O}_6$ in the $P\bar{3}1m$ structure.

	a (Å)	c (Å)	x_p	x_s	z_s
$\text{Li}_4\text{P}_2\text{S}_6$ (exp)	6.070	6.577	0.1715	0.3237	0.2500
$\text{Li}_4\text{P}_2\text{S}_6$ (cal)	5.96	6.37	0.1758	0.3314	0.2483
$\text{Li}_4\text{P}_2\text{O}_6$ (cal)	4.78	5.37	0.1951	0.3139	0.2615

they could be estimated from a related material [36]. In the case of $\text{Li}_6\text{PS}_5\text{Cl}$, the calculated results are compared with the detailed measurements for $\text{Li}_6\text{PS}_5\text{I}$, which is expected to be similar.

3.3. $\text{Li}_4\text{P}_2\text{S}_6$ and $\text{Li}_4\text{P}_2\text{O}_6$

The crystal structure of $\text{Li}_4\text{P}_2\text{S}_6$ was described by Mercier et al. [39] as hexagonal $P6_3/mcm$ (#193) with half occupancy of the P (4e) sites. Our electronic structure calculations of the 6 possible configurations of this unit cell find the lowest energy structure to be described by the $P\bar{3}1m$ (#162) structure which is a subgroup of the original space group. In this hexagonal group, the Li ions are located at $2c$ (1/3, 2/3, 0) and $2d$ (1/3, 2/3, 1/2) sites, the P ions are located at $2e$ (0, 0, z_p) sites, and the S ions are located at $6k$ (x_s , 0, z_s) sites. The calculated lattice constants and fractional coordinate parameters are listed in Table 3 along with the corresponding experimental results. We were also able to simulate a meta-stable phosphate material with the same structure; the optimized lattice parameters for $\text{Li}_4\text{P}_2\text{O}_6$ are also listed in Table 3.

In contrast to the other phosphates and thiophosphates, an interesting characteristic of the optimized $\text{Li}_4\text{P}_2\text{S}_6$ and $\text{Li}_4\text{P}_2\text{O}_6$ structures is the presence of a direct bond between two P ions. In $\text{Li}_4\text{P}_2\text{S}_6$ the P–P bond length is 2.24 Å which is 10% longer than the P–S bond length, while in $\text{Li}_4\text{P}_2\text{O}_6$ the P–P bond length is 2.10 Å which is 40% longer than the P–O bond length. This is illustrated in Fig. 3.

3.4. $\text{Li}_4\text{P}_2\text{S}_7$ and $\text{Li}_4\text{P}_2\text{O}_7$

While to the best of our knowledge, the crystal structure of $\text{Li}_4\text{P}_2\text{S}_7$ is unknown, $\text{Li}_4\text{P}_2\text{O}_7$ was found to crystallize [40] in the $P1$ structure (#2). Our simulations confirm this structure [9] and simulations for the corresponding thiophosphate – $\text{Li}_4\text{P}_2\text{S}_7$ – show that it has at least a meta-stable state in the same structure. Table 4 summarizes the lattice parameters for these structures and Fig. 4 shows ball and stick models of the unit cell for these structures.

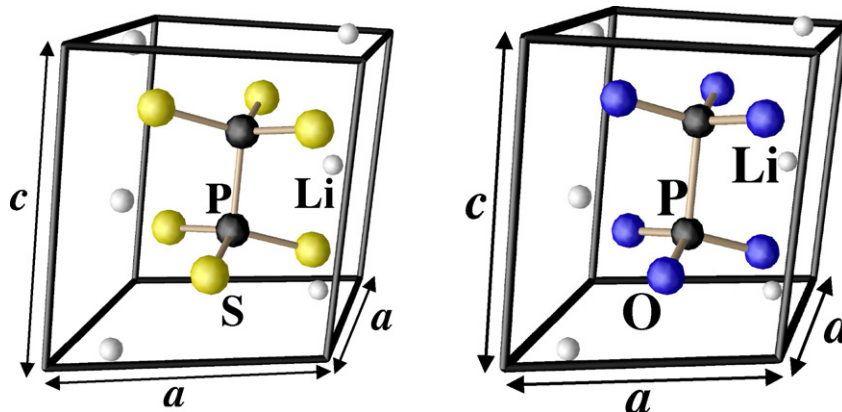


Fig. 3. Ball and stick diagrams for unit cells of $\text{Li}_4\text{P}_2\text{S}_6$ (left) and $\text{Li}_4\text{P}_2\text{O}_6$ (right) in the $P\bar{3}1m$ structure.

Table 4Lattice parameters for $\text{Li}_4\text{P}_2\text{O}_7$ and $\text{Li}_4\text{P}_2\text{S}_7$ in the $P\bar{1}$ structure, comparing experimental results (“exp”) of Ref. [40] with optimized structures (“cal”) found in this work.

	a (Å)	b (Å)	c (Å)	α	β	γ
$\text{Li}_4\text{P}_2\text{O}_7$ (exp)	8.56	7.11	5.19	111.4°	90.0°	103.1°
$\text{Li}_4\text{P}_2\text{O}_7$ (cal)	8.40	7.01	5.13	111.7°	90.0°	103.6°
$\text{Li}_4\text{P}_2\text{S}_7$ (cal)	10.67	8.81	5.80	111.1°	89.9°	90.8°

Atom	Fractional coordinates – (x, y, z)		
	$\text{Li}_4\text{P}_2\text{O}_7$ (exp)	$\text{Li}_4\text{P}_2\text{O}_7$ (cal)	$\text{Li}_4\text{P}_2\text{S}_7$ (cal)
Li (1)	(0.791, 0.673, 0.644)	(0.788, 0.677, 0.653)	(0.854, 0.647, 0.476)
Li (2)	(0.452, 0.755, 0.702)	(0.444, 0.745, 0.699)	(0.489, 0.751, 0.689)
Li (3)	(0.754, 0.412, 0.016)	(0.763, 0.422, 0.027)	(0.679, 0.478, –0.133)
Li (4)	(0.988, 0.854, 0.110)	(0.987, 0.855, 0.106)	(1.012, 0.880, 0.149)
P (1)	(0.846, 0.222, 0.438)	(0.850, 0.227, 0.444)	(0.801, 0.216, 0.450)
P (2)	(0.631, –0.214, 0.214)	(0.626, –0.216, 0.215)	(0.685, –0.189, 0.254)
O/S (1)	(0.684, 0.038, 0.308)	(0.680, 0.042, 0.315)	(0.676, 0.040, 0.203)
O/S (2)	(0.875, 0.259, 0.741)	(0.882, 0.268, 0.752)	(0.796, 0.231, 0.800)
O/S (3)	(0.794, 0.398, 0.390)	(0.798, 0.407, 0.394)	(0.713, 0.413, 0.417)
O/S (4)	(0.982, 0.151, 0.270)	(0.985, 0.149, 0.268)	(0.975, 0.173, 0.301)
O/S (5)	(0.622, –0.261, 0.476)	(0.618, –0.264, 0.482)	(0.689, –0.158, 0.612)
O/S (6)	(0.472, –0.270, 0.047)	(0.463, –0.276, 0.045)	(0.529, –0.299, 0.071)
O/S (7)	(0.763, –0.297, 0.041)	(0.763, –0.296, 0.041)	(0.839, –0.309, 0.080)

3.5. $\text{Li}_7\text{P}_3\text{S}_{11}$

The crystal structure of the superionic conductor $\text{Li}_7\text{P}_3\text{S}_{11}$ was recently analyzed by Yumane et al. [13] who found it has $P\bar{1}$ symmetry (#2). The measured and calculated lattice parameters are listed in Table 5. It is interesting that the calculated value of the b lattice parameter is larger than experiment while the a and c lattice parameters follow the usual trend of being smaller than experiment. The calculated fractional coordinates are generally in good agreement with the experimental values. Yumane et al. have shown that this structure is composed of an ordered arrangement of $\text{Li}_4\text{P}_2\text{S}_7$ and Li_3S_4 groups similar to the structures seen in Figs. 4 and 1.

4. Heats of formation

In order to assess the chemical stability of the materials, we estimated the heats of formation relative to their decomposition to elemental materials in their standard states as defined in the CRC Handbook [41], using the methods described in our earlier work [9]. In order to extend the analysis to sulfur containing materials we needed to estimate the equilibrium energy of the standard state of elemental S, which is the orthorhombic form ($\alpha\text{-S}_8$) [42] having the structure $Fddd$ (#70). In order to extend the analysis to Cl-containing materials, we needed to estimate the energy of the standard state of elemental Cl, which is molecular Cl_2 . Instead

of evaluating this energy directly, we estimated it from the total energies of LiCl in the rocksalt structure, LiClO_4 in the $Pnma$ (#62) structure [43], and PCl_5 in the $P4/n$ (#85) structure [44] and the heat of formation data values for these materials given in the CRC Handbook [41].

Some results are given in Table 6 where a few results are repeated from Ref. [9]. From our previous experience and from the accuracy of finding the standard energy of elemental chlorine, we expect that the error of the calculation to be ± 0.5 eV although the relative error between materials of similar composition is expected to be considerably less.

In addition to the phosphate and thiophosphate materials, the reference materials Li_2O , Li_2S , LiCl , LiClO_4 , and PCl_5 are also listed.

From these results, we can make some comments on relative stabilities of these materials. For example, the calculations suggest that $\text{Li}_4\text{P}_2\text{S}_6$ is more stable than $\text{Li}_4\text{P}_2\text{S}_7$ in the sense that in their standard states:

$$\Delta H(\text{Li}_4\text{P}_2\text{S}_6) + \Delta H(\text{S}) = \Delta H(\text{Li}_4\text{P}_2\text{S}_7) - 0.84 \text{ eV}. \quad (1)$$

In fact there are literature reports of glassy $\text{Li}_4\text{P}_2\text{S}_7$, but we know of no reports of crystalline $\text{Li}_4\text{P}_2\text{S}_7$. By contrast, for the analogous phosphate materials, we find

$$\Delta H(\text{Li}_4\text{P}_2\text{O}_6) + \frac{1}{2} \Delta H(\text{O}_2) = \Delta H(\text{Li}_4\text{P}_2\text{O}_7) + 4.21 \text{ eV}, \quad (2)$$

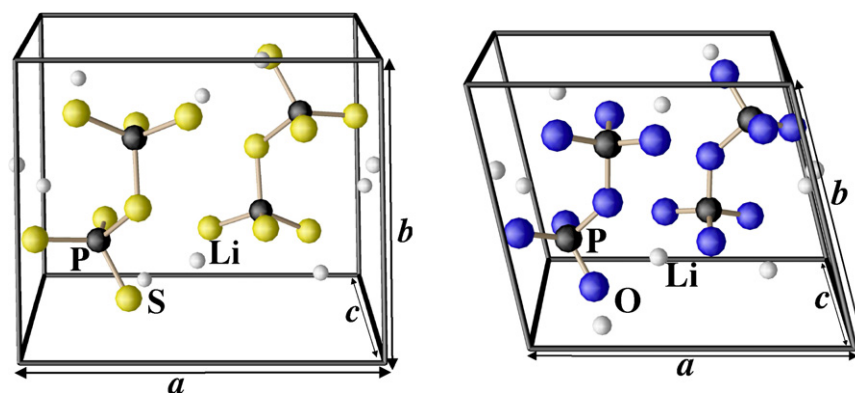


Fig. 4. Ball and stick diagrams for unit cells of $\text{Li}_4\text{P}_2\text{S}_7$ (left) and $\text{Li}_4\text{P}_2\text{O}_7$ (right) in the $P\bar{1}$ structure.

Table 5

Lattice parameters for $\text{Li}_7\text{P}_3\text{S}_{11}$ in the $P\bar{1}$ structure, comparing experimental results ("exp") of Ref. [13] with optimized structures ("cal") found in this work.

	a (Å)	b (Å)	c (Å)	α	β	γ
$\text{Li}_7\text{P}_3\text{S}_{11}$ (exp)	12.50	6.03	12.53	102.8°	113.2°	74.5°
$\text{Li}_7\text{P}_3\text{S}_{11}$ (cal)	12.00	6.16	12.24	102.4°	113.8°	72.1°
Fractional coordinates – (x, y, z)						
Atom	$\text{Li}_7\text{P}_3\text{S}_{11}$ (cal)		$\text{Li}_7\text{P}_3\text{S}_{11}$ (cal)			
Li (1)	(0.669, 0.132, 0.092)	(0.669, 0.070, 0.094)				
Li (2)	(0.638, 0.402, 0.866)	(0.600, 0.549, 0.880)				
Li (3)	(0.216, 0.530, 0.740)	(0.199, 0.489, 0.707)				
Li (4)	(–0.058, 0.786, 0.270)	(–0.030, 0.837, 0.251)				
Li (5)	(0.359, 0.591, 0.337)	(0.299, 0.771, 0.298)				
Li (6)	(0.637, 0.734, 0.498)	(0.680, 0.648, 0.508)				
Li (7)	(0.139, 0.294, 0.134)	(0.129, 0.268, 0.116)				
P (1)	(0.794, 0.033, 0.465)	(0.780, 0.054, 0.452)				
P (2)	(0.493, 0.038, 0.297)	(0.472, –0.007, 0.273)				
P (3)	(0.840, 0.270, 0.059)	(0.830, 0.318, 0.057)				
S (1)	(0.861, 0.236, 0.620)	(0.822, 0.289, 0.598)				
S (2)	(0.824, 0.105, 0.334)	(0.811, 0.118, 0.314)				
S (3)	(0.840, –0.317, 0.468)	(0.853, –0.271, 0.488)				
S (4)	(0.618, 0.160, 0.453)	(0.583, 0.170, 0.425)				
S (5)	(0.331, 0.227, 0.288)	(0.304, 0.152, 0.294)				
S (6)	(0.509, 0.080, 0.151)	(0.478, 0.047, 0.120)				
S (7)	(0.509, –0.300, 0.307)	(0.522, –0.343, 0.302)				
S (8)	(0.841, 0.330, –0.097)	(0.820, 0.394, –0.102)				
S (9)	(0.828, –0.073, 0.046)	(0.865, –0.028, 0.057)				
S (10)	(0.678, 0.487, 0.064)	(0.663, 0.474, 0.081)				
S (11)	(0.977, 0.351, 0.188)	(0.968, 0.429, 0.203)				

suggesting that $\text{Li}_4\text{P}_2\text{O}_6$ is significantly unstable relative to $\text{Li}_4\text{P}_2\text{O}_7$. In fact we know of no literature reports of observations of $\text{Li}_4\text{P}_2\text{O}_6$ crystals.

For the argyrodite material, the calculations also suggest that Li_7PS_6 is unstable relative to decomposition into Li_3PS_4 and Li_2S in the sense that

$$\Delta H(\text{Li}_7\text{PS}_6) = \Delta H(\text{Li}_3\text{PS}_4) + 2\Delta H(\text{Li}_2\text{S}) + 0.32 \text{ eV}. \quad (3)$$

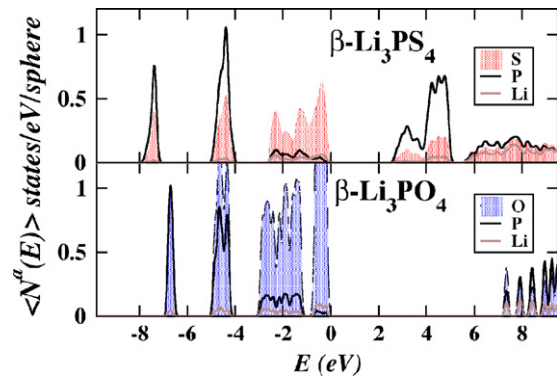
In this estimate, we used the $\beta\text{-Li}_3\text{PO}_4$ structure to evaluate $\Delta H(\text{Li}_3\text{PS}_4)$ and the result is within our expected calculation error. The material with chlorine is also marginally unstable relative to decomposition into Li_3PS_4 , Li_2S , and LiCl as shown in the equation

$$\Delta H(\text{Li}_6\text{PS}_5\text{Cl}) = \Delta H(\text{Li}_3\text{PS}_4) + \Delta H(\text{Li}_2\text{S}) + \Delta H(\text{LiCl}) + 0.38 \text{ eV}. \quad (4)$$

Table 6

Heats of formation per formula unit calculated for the listed reference and lithium phosphate and thiophosphate materials. The structure is described in terms of the space group using the notation of Ref. [31]. When available, experimental values of ΔH from Ref. [41] are also listed.

Material	Structure	ΔH_{cal} (eV)	ΔH_{exp} (eV)
Li_2O	$Fm\bar{3}m$ (#225)	–6.13	–6.20
$\beta\text{-Li}_3\text{PO}_4$	$Pmn2_1$ (#31)	–21.31	
$\gamma\text{-Li}_3\text{PO}_4$	$Pnma$ (#62)	–21.28	–21.72
$\text{Li}_4\text{P}_2\text{O}_7$	$P\bar{1}$ (#2)	–34.10	
$\text{Li}_4\text{P}_2\text{O}_6$	$P\bar{3}1m$ (#162)	–29.89	
Li_2S	$Fm\bar{3}m$ (#225)	–4.26	–4.57
$\beta\text{-Li}_3\text{PS}_4$	$Pmn2_1$ (#31)	–8.32	
$\gamma\text{-Li}_3\text{PS}_4$	$Pnma$ (#62)	–8.12	
Li_7PS_6	$Pna2_1$ (#33)	–16.51	
$\text{Li}_4\text{P}_2\text{S}_7$	$P\bar{1}$ (#2)	–11.51	
$\text{Li}_4\text{P}_2\text{S}_6$	$P\bar{3}1m$ (#162)	–12.35	
$\text{Li}_7\text{P}_3\text{S}_{11}$	$P\bar{1}$ (#2)	–19.89	
LiCl	$Fm\bar{3}m$ (#225)	–3.80	–4.23
LiClO_4	$Pnma$ (#62)	–4.49	–3.95
PCl_5	$P4/m$ (#85)	–4.08	–4.60
$\text{Li}_6\text{PS}_5\text{Cl}$	Cc (#9)	–16.00	

**Fig. 5.** Partial densities of states for Li_3PS_4 and Li_3PO_4 .

The calculations also suggest that $\text{Li}_7\text{P}_3\text{S}_{11}$ is marginally stable with respect to decomposition into Li_3PS_4 and $\text{Li}_4\text{P}_2\text{S}_7$ in the sense that

$$\Delta H(\text{Li}_7\text{P}_3\text{S}_{11}) = \Delta H(\text{Li}_3\text{PS}_4) + \Delta H(\text{Li}_4\text{P}_2\text{S}_7) - 0.06 \text{ eV}. \quad (5)$$

Again, this is within the expected calculational error.

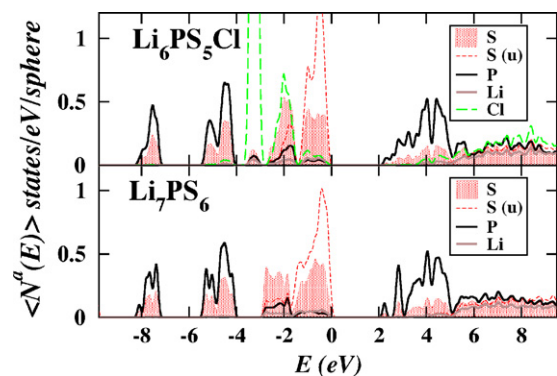
5. Partial densities of states

The partial densities of states can be evaluated using the form

$$N^a(E) = \frac{1}{\sqrt{\pi}\Delta} \sum_{nk} f_{nk}^a W_k e^{-(E-E_{nk})^2/\Delta^2}. \quad (6)$$

Here the smearing factor was chosen to be $\Delta = 0.1 \text{ eV}$. W_k denotes the Brillouin zone sampling factor. f_{nk}^a denotes the weighting factor which for each state of band index n and wave vector k , was taken to be the corresponding charge within the atomic sphere at site a . The sphere radii were chosen to be 1.4 bohr for O and S, 1.5 bohr for P and Cl, and 1.6 bohr for Li. In practice, the partial densities of state for each atomic site are averaged over all similar sites, $\langle N^a(E) \rangle$. These averaged partial densities of states contain qualitative information about the materials in terms of charge transfers, crystal field splittings, and bond formation. In all of the phosphates, the bands are dominated by the 2p states of O while for the thiophosphates, the bands are dominated by the 3p bands of S.

We first consider materials composed of isolated phosphate and thiophosphate groups. In Fig. 5 the partial densities of states of Li_3PS_4 and Li_3PO_4 are compared. The S 3p valence bands of Li_3PS_4 cover a wider range of energies than the O 2p valence bands of Li_3PO_4 . As noted in our earlier work [6] the two lower bands have $p\sigma$ character with significant hybridization with the P 3s and 3p states, while the top of the valence band has $p\pi$ character. It is

**Fig. 6.** Partial densities of states for Li_7PS_6 and $\text{Li}_6\text{PS}_5\text{Cl}$. Contributions from unbounded S sites are indicated with "(u)".

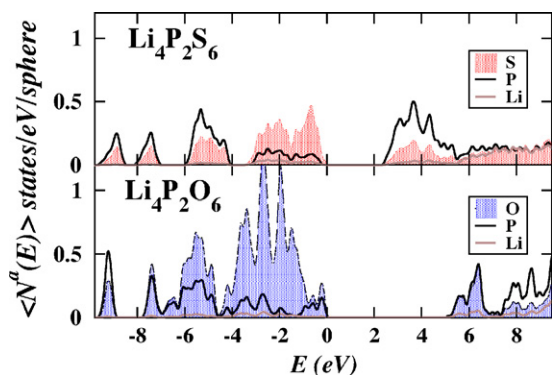


Fig. 7. Partial densities of states for $\text{Li}_4\text{P}_2\text{S}_6$ and $\text{Li}_4\text{P}_2\text{O}_6$.

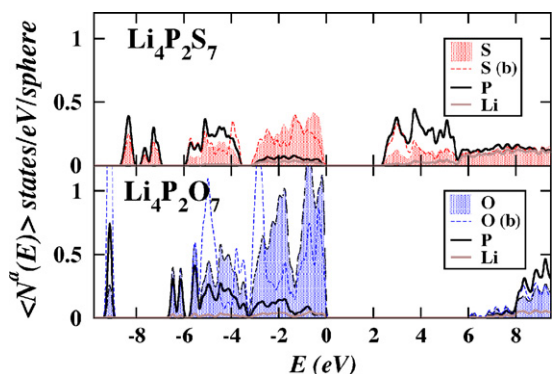


Fig. 8. Partial densities of states for $\text{Li}_4\text{P}_2\text{S}_7$ and $\text{Li}_4\text{P}_2\text{O}_7$. Contributions from bridging S or O sites are indicated with “(b)”.

interesting to note that the magnitudes of the O contributions to $\langle N^d(E) \rangle$ the partial densities of states are generally larger than those of S, indicating that the charge of the O $2p$ states is more confined within the analysis sphere than the charge of the S $3p$ states. While the calculated band gaps within density functional theory are systematically underestimated, it is clear that the gap in Li_3PS_4 is less than half of that in Li_3PO_4 .

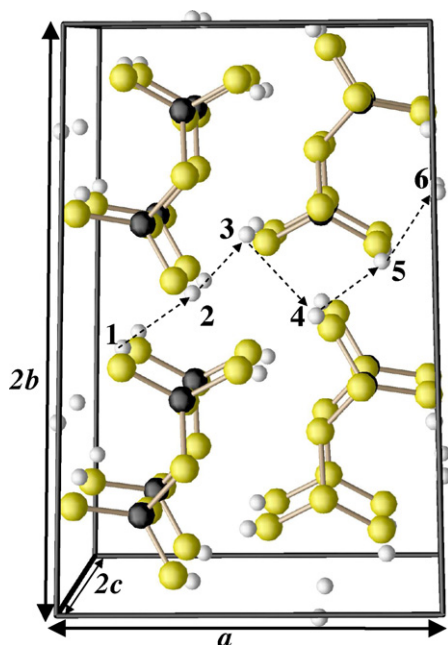


Fig. 9. Li ion vacancy sites used in migration energy study in $\text{Li}_4\text{P}_2\text{S}_7$. Similar sites were used for $\text{Li}_4\text{P}_2\text{O}_7$.

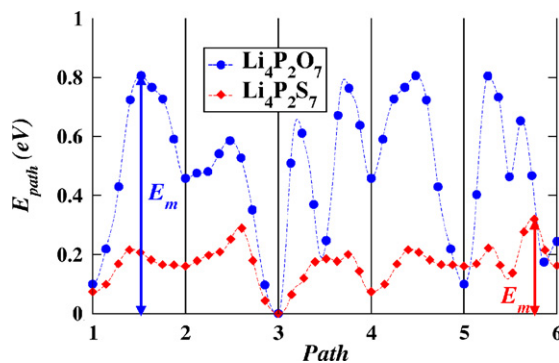


Fig. 10. Energy path diagram for Li ion vacancy migration in $\text{Li}_4\text{P}_2\text{S}_7$ and $\text{Li}_4\text{P}_2\text{O}_7$. The integer labels on the horizontal axis correspond to the 6 vacancy sites indicated in the structural diagram (Fig. 9). Between each pair of optimized vacancy configurations are 7 NEB image configurations along the minimum energy path.

Next we consider the partial densities of states of the argyrodite structured thiophosphates, comparing the partial densities of states of Li_7PS_6 and $\text{Li}_6\text{PS}_5\text{Cl}$ in Fig. 6. For Li_7PS_6 , the partial density of states contribution from isolated S ions (indicated separately from the tetrahedrally bonded S's) are found to contribute relatively narrow bands near the top of the valence band. For $\text{Li}_6\text{PS}_5\text{Cl}$, the isolated Cl ion contributions are at lower energy than those of the isolated S ions.

In Figs. 7 and 8 densities of states for $\text{Li}_4\text{P}_2\text{O}_6$ and $\text{Li}_4\text{P}_2\text{S}_6$ and $\text{Li}_4\text{P}_2\text{O}_7$ and $\text{Li}_4\text{P}_2\text{S}_7$ are compared. For $\text{Li}_4\text{P}_2\text{O}_6$ and $\text{Li}_4\text{P}_2\text{S}_6$, one additional valence band is present due to the filled P $3s\sigma$ bond, whose contribution is concentrated near the bottom of the spectrum. In contrast, for $\text{Li}_4\text{P}_2\text{O}_7$ and $\text{Li}_4\text{P}_2\text{S}_7$, while states with contributions from the P site contribute throughout the valence band, there is no additional valence state due to filled P states. On the other hand there are two types of O (S) states. In addition to the normal tetrahedral O (S) site contributions, the “bridging” O (S) site contributions are shown separately on the plot. In particular, there is a band at the bottom of the valence band states which corresponds to states characterized primarily by O $2p\sigma$ or S $3p\sigma$ contributions for $\text{Li}_4\text{P}_2\text{O}_7$ and $\text{Li}_4\text{P}_2\text{S}_7$, respectively.

6. Li ion migration energies

An important question about these materials is how the Li ion migration differs in the phosphate and thiophosphate materials. The ionic conductivity σ as a function temperature T is expected to follow the Arrhenius relation:

$$\sigma \cdot T = Kn e^{-E_m/kT}, \quad (7)$$

where k is the Boltzmann constant, K is a material-dependent parameter, n is the concentration of mobile Li ions or Li ion vacancies, and E_m is the migration energy.

In this initial study, we focus on the migration energy E_m for Li ion vacancy migration in idealized crystals of $\text{Li}_4\text{P}_2\text{O}_7$ and $\text{Li}_4\text{P}_2\text{S}_7$. As discussed in Section 3, these two materials form similar stable and meta-stable crystals with $P\bar{1}$ symmetry. For the simulations, we constructed $1 \times 2 \times 2$ supercells and studied the migration of a Li ion vacancy between 6 sites separated by roughly 3.0\AA and 3.6\AA for $\text{Li}_4\text{P}_2\text{O}_7$ and $\text{Li}_4\text{P}_2\text{S}_7$, respectively. The sites do not span a complete path within the supercell but do cover a representative range of crystal environments. The 6 sites are illustrated in Fig. 9 for the $\text{Li}_4\text{P}_2\text{S}_7$ supercell.

The band occupancies of the supercell states were adjusted in order to approximate an insulating environment for ion migration, and the excess charge was compensated by adding a uniform charge of the opposite sign. The 6 optimized configurations for a Li ion vacancy were used as the end points for the NEB calculation in

which 7 intermediate images were used to approximate the minimum energy path. As is evident from the energy path diagram shown in Fig. 10, the energy landscape for this system is complicated. However, the results indicate a clear qualitative result that the migration energy barriers for Li ion vacancy migration in $\text{Li}_4\text{P}_2\text{S}_7$ is less than half that in $\text{Li}_4\text{P}_2\text{O}_7$. For the particular migration path chosen, we find the migration energy barriers to be $E_m = 0.3$ eV for $\text{Li}_4\text{P}_2\text{S}_7$ and $E_m = 0.8$ eV for $\text{Li}_4\text{P}_2\text{O}_7$.

7. Summary and conclusions

This study has found some interesting similarities and differences between the phosphate and thiophosphate materials. Our structural optimizations were generally in good agreement with the experimental structures, although there were some obvious differences. For example, our calculations for Li_3PS_4 indicated that the most stable structure is that of $\beta\text{-Li}_3\text{PO}_4$, while the experiment [34] indicated a form with the same space group as $\gamma\text{-Li}_3\text{PO}_4$ with partial occupancies of some of the sites. A similar discrepancy was found for the structure of $\text{Li}_4\text{P}_2\text{S}_6$ [39]. These differences are undoubtedly related to real temperature effects which are not considered in the simulations.

In general, a greater variety in the bonding configurations of the thiophosphates is observed compared with those of the phosphates. The argyrodite structures [35,36] with unbounded S and Cl groups within the crystal and increased concentrations of Li ions are very intriguing. The density of states plots shown in Fig. 6 indicate that the unbounded S states contribute to the top of the valence band. The corresponding states associated with unbounded Cl sites have lower energy than those of the unbound S sites. The heats of formation for these materials suggest that they may be unstable relative to decomposition, although the uncertainty of our estimates do not allow a definitive analysis.

In addition to our analysis of the stability of structures and stabilities, we have presented some preliminary results pertaining to Li ion vacancy migration within a representative set of materials. We find that the energy barriers for Li ion vacancy migration in $\text{Li}_4\text{P}_2\text{S}_7$ to be less than half that for $\text{Li}_4\text{P}_2\text{O}_7$. This result is consistent with the experimental observation of increased ionic conductivity in the thiophosphate materials compared with those of the phosphates. Our analysis suggests that one factor contributing to the lowered potential barriers in the thiophosphates is the more diffuse valence charge distribution near the S sites compared with the compact valence charge distribution near the O sites.

We are looking forward to further simulations related to this intriguing class of materials, hopefully with collaboration with experimental studies.

Acknowledgments

This work was supported by NSF grants DMR-0427055 and 0705239 and by the Wake Forest University DEAC computer cluster. We would like to thank Dr. F. Stadler for informing us about the argyrodite materials.

References

- [1] J.B. Bates, N.J. Dudney, G.R. Gruzalski, R.A. Zuhr, A. Choudhury, D.F. Luck, J.D. Robertson, *Solid State Ionics* 53–56 (1992) 647–654.

- [2] B. Wang, B.C. Chakoumakos, B.C. Sales, B.S. Kwak, J.B. Bates, *J. Solid State Chem.* 115 (1995) 313–323.
- [3] X. Yu, J.B. Bates, J.G.E. Jellison, F.X. Hart, *J. Electrochem. Soc.* 144 (1997) 524–532.
- [4] N.J. Dudney, *Interface* 17 (3) (2008) 44–48.
- [5] Y.A. Du, N.A.W. Holzwarth, *J. Electrochem. Soc.* 154 (2007) A999–A1004.
- [6] Y.A. Du, N.A.W. Holzwarth, *Phys. Rev. B* 76 (2007), 174302 (14 pp).
- [7] Y.A. Du, N.A.W. Holzwarth, *Phys. Rev. B* 78 (2008), 174301 (13 pp).
- [8] Y.A. Du, N.A.W. Holzwarth, *ECS Trans.* 13 (2008) 75–82.
- [9] Y.A. Du, N.A.W. Holzwarth, *Phys. Rev. B* 81 (2010) 184106 (15 pp).
- [10] F. Mizuno, A. Hayashi, K. Tadanaga, M. Tatsumisago, *Electrochem. Solid-State Lett.* 8 (2005) A603–A606.
- [11] F. Mizuno, A. Hayashi, K. Tadanaga, M. Tatsumisago, *Adv. Mater.* 17 (2005) 918–921.
- [12] F. Mizuno, T. Ohtomo, A. Hayashi, K. Tadanaga, M. Tatsumisago, *Solid State Ionics* 177 (2006) 2753–2757.
- [13] H. Yamane, M. Shibata, Y. Shimane, T. Junke, Y. Seino, S. Adams, K. Minami, A. Hayashi, M. Tatsumisago, *Solid State Ionics* 178 (2007) 1163–1167.
- [14] A. Hayashi, *J. Ceram. Soc. Jpn.* 115 (2007) 110–117.
- [15] M. Tatsumisago, A. Hayashi, *J. Non-Cryst. Solids* 354 (2008) 1411–1417.
- [16] K. Minami, A. Hayashi, M. Tatsumisago, *Solid State Ionics* 179 (2008) 1282–1285.
- [17] A. Hayashi, K. Minami, F. Mizuno, M. Tatsumisago, *J. Mater. Sci.* 43 (2008) 1885–1889.
- [18] A. Hayashi, K. Minami, M. Tatsumisago, *J. Non-Cryst. Solids* 355 (2009) 1919–1923.
- [19] J. Trevey, J.S. Jang, Y.W. Jung, C.R. Stoldt, S.-H. Lee, *Electrochem. Commun.* 11 (2009) 1830–1833.
- [20] P. Hohenberg, W. Kohn, *Phys. Rev.* 136 (1964) B864–B871.
- [21] W. Kohn, L.J. Sham, *Phys. Rev.* 140 (1965) A1133–A1138.
- [22] J.P. Perdew, Y. Wang, *Phys. Rev. B* 45 (1992) 13244–13249.
- [23] P. Giannozzi, S. Baroni, N. Bonini, M. Calandra, R. Car, C. Cavazzoni, D. Ceresoli, G.L. Chiarotti, M. Cococcioni, I. Dabo, A.D. Corso, S. de Gironcoli, S. Fabris, G. Fratesi, R. Gebauer, U. Gerstmann, C. Gougousis, A. Kokalj, M. Lazzeri, L. Martin-Samos, N. Marzari, F. Mauri, R. Mazzarello, S. Paolini, A. Pasquarello, L. Paulatto, C. Sbraccia, S. Scandolo, G. Sclauzero, A.P. Seitsonen, A. Smogunov, P. Umari, R.M. Wentzcovitch, *J. Phys.: Condens. Matter* 21 (2009) 394402 (19 pp). Available from the website <http://www.quantum-espresso.org>.
- [24] X. Gonze, G.M. Rignanese, M. Verstraete, J.-M. Beuken, Y. Pouillon, R. Caracas, F. Jollet, M. Torrent, G. Zerah, M. Mikami, P. Ghosez, M. Veithen, J.-Y. Raty, V. Olevano, F. Bruneval, F. Mauri, R. Godby, G. Onida, D.R. Hamann, D.C. Allan, *Z. Kristallogr.* 220 (2005) 558–562, Available from the website <http://www.abinit.org>.
- [25] A.R. Tackett, N.A.W. Holzwarth, G.E. Matthews, *Comput. Phys. Commun.* 135 (2001) 348–376, Available from the website <http://pwpaw.wfu.edu>.
- [26] OpenDX – The Open Source Software Project Based on IBM's Visualization Data Explorer – is available from the web site <http://www.opendx.org>.
- [27] A. Kokalj, *J. Mol. Graph. Model.* 17 (1999) 176–179.
- [28] H. Jónsson, G. Mills, K.W. Jacobsen, in: B.J. Berne, G. Ciccotti, D.F. Coker (Eds.), *Classical and Quantum Dynamics in Condensed Phase Simulations*, World Scientific, Singapore, 1998, pp. 385–404.
- [29] G. Henkelman, B.P. Uberuaga, H. Jónsson, *J. Chem. Phys.* 113 (2000) 9901–9904.
- [30] G. Henkelman, H. Jónsson, *J. Chem. Phys.* 113 (2000) 9978–9985.
- [31] T. Hahn (Ed.), *International Tables for Crystallography, Vol. A: Space-group Symmetry*, Fifth revised edition, Kluwer, 2002, ISBN 0-7923-6590-9, The symmetry labels used in this work are all based on this reference.
- [32] C. Keffer, A. Mighell, F. Mauer, H. Swanson, S. Block, *Inorg. Chem.* 6 (1967) 119–125.
- [33] O.V. Yakubovich, V.S. Urusov, *Crystallogr. Rep.* 42 (1997) 261–268.
- [34] R. Mercier, J.-P. Malugani, B. Fahyst, G. Robert, *Acta Crystallogr. B* 38 (1982) 1887–1890.
- [35] S.T. Kong, Ö. Gün, B. Koch, H.J. Deiseroth, H. Eckert, C. Reiner, *Chem. Eur. J.* 16 (2010) 5138–5147.
- [36] S.T. Kong, H.J. Deiseroth, C. Reiner, Ö. Gün, E. Neumann, C. Ritter, D. Zahn, *Chem. Eur. J.* 16 (2010) 2198–2206.
- [37] H.-J. Deiseroth, S.-T. Kong, H. Eckert, J. Vannahme, C. Reiner, T. Zaiß, M. Schlosser, *Angew. Chem. Int. Ed.* 47 (2008) 755–758.
- [38] F. Stadler, C. Fietzek, *ECS Trans.* 25 (2010) 177–183.
- [39] R. Mercier, J.P. Malugani, B. Fays, J. Douglade, G. Robert, *J. Solid State Chem.* 43 (1982) 151–162.
- [40] A. Daidouh, M.L. Veiga, C. Pico, M. Martinez-Ripoll, *Acta Crystallogr. C* 53 (1997) 167–169.
- [41] D.R. Lide (Ed.), *CRC Handbook of Chemistry and Physics*, 90th ed., CRC Press, Taylor & Francis Group, 2009, ISBN 978-1-4200-9084-0.
- [42] S.J. Rettig, J. Trotter, *Acta Crystallogr. C* 43 (1987) 2260–2262.
- [43] K.D.M. Harris, M. Tremayne, *Chem. Mater.* 8 (1996) 2554–2570.
- [44] D. Clark, H.M. Powell, A.F. Wells, *J. Chem. Soc.* 134 (1942) 642–645.